Vertical Co9S8 hollow nanowall arrays grown on Celgard separator as a multifunctional polysulfide barrier for high-performance Li-S batteries

Journal:	*Energy & Environmental Science*
Manuscript ID	EE-ART-03-2018-000893.R1
Article Type:	Paper
Date Submitted by the Author:	11-Jun-2018
Complete List of Authors:	He, Jiarui; University of Texas at Austin, Materials Science and Engineering Chen, Yuanfu; State Key Laboratory of Electronic Thin Films and Integrated Devices, University of Electronic Science and Technology of China Manthiram, Arumugam; University of Texas at Austin, Materials Science and Engineering

Journal Name

ARTICLE

Vertical Co_9S_8 hollow nanowall arrays grown on Celgard separator as a multifunctional polysulfide barrier for high-performance Li-S batteries

Received 00th January 20xx,
Accepted 00th January 20xx

DOI: 10.1039/x0xx00000x

www.rsc.org/

Jiarui He,[a,b] Yuanfu Chen,[b,*] and Arumugam Manthiram[a,*]

Lithium-sulfur (Li-S) batteries have been regarded as one of the most promising next-generation energy-storage devices, due to their low cost and high theoretical energy density (2600 W h kg^{-1}). However, the severe dissolution of lithium polysulfides (LiPSs) and fatal shuttle effect of sulfur cathode seriously hinder the practical applications of Li-S batteries. To address such issues, we present here, for the first time, a novel metal organic framework (MOF)-derived Co_9S_8 nanowall array with vertical hollow naoarchitecture and high electrical conductivity, which are *in-situ* grown on Celgard separator (Co_9S_8-Celgard) via a feasible and scalable liquid-reaction approach, as an efficient barrier for LiPSs in Li-S batteries. Benefiting from the direct *in-situ* growth of vertial Co_9S_8 hollow nanowall arrays as a multifunctional polar barrier, the Co_9S_8-Celgard separator possesses large surface area, excellent mechanical stability, and particularly strong LiPSs-trapping ability *via* chemical and physical interaction. With these advantages, even with a pure sulfur cathode with a high sulfur loading of 5.6 mg cm^{-2}, the Li-S cells with the Co_9S_8-Celgard separator exhibit outstanding electrochemical performances: the initial specific capacity is as high as 1,385 mA h g^{-1} with a retention of 1,190 mA h g^{-1} after 200 cycles; the cells deliver a high capacity of 530 mA h g^{-1} at 1C rate (1,675 mA g^{-1}) even after an impressive number of 1,000 cycles with an average capacity fading of only 0.039% per cycle, which is promising for long-term cycling application at high charge/discharge current densities; and pouch-type Li-S cells with the Co_9S_8-Celgard separator display excellent cycling performance. When the optimized cathode with the sulfur loading in well-designed yolk-shelled carbon@Fe_3O_4 (YSC@Fe_3O_4) nanoboxes is employed, the cell with Co_9S_8-Celgard delivers a high initial capacity of 986 mA h g^{-1} at 1C rate with a capacity retention of as high as 83.2 % even after a remarkable number of 1,500 cycles. The work presents a strategy to growon the separator a multifunctional polar interlayer with unique nanoarchitecture and high conductivity to chemically and physically trap the LiPSs, thus significantly enhancing the performance of Li-S batteries.

Broader context

Advanced energy-storage technologies are urgently needed to satisfy the energy demands of the society. Sulfur is an appealing candidate for high energy-density batteries, owing to its high theoretical capacity (1,675 mA h g^{-1}), natural abundance, and low cost. However, the rapid capacity degradation, low Coulombic efficiency, and short cycle life originating from polysulfide dissolution and migration remain challenging for the practical application of lithium-sulfur (Li-S) batteries. We present here an interlayer with well-aligned hollow Co_9S_8 arrays *in-situ* grown on a Celgard separator as an efficient polysulfide barrier for high-performance Li-S cells. The presented concept/strategy of designing a multifunctional separator via *in-situ* grown polar and conductive materials (Co_9S_8 arrays) on commercial separator is novel and significant to dramatically improve the electrochemical performance of Li-S cells. Due to its well-designed structure, *in-situ* growth/transformation, and the polarity and high conductivity of Co_9S_8, the Li-S cell with the Co_9S_8-Celgard separator not only effectively blocks the lithium polysulfides (LiPSs) even with pure sulfur cathodes with a very high sulfur loading (5.6 mg cm^{-2}), but also delivers excellent specific capacity, outstanding rate capacity, and pronounced cycling stability for an impressive number of 1,000 cycles. More importantly, the multifunctional Co_9S_8-Celgard separator also shows excellent electrochemical performance in a pouch cell, demonstrating that the Co_9S_8-Celgard separator is promising for practical applications.

Introduction

The limited capacity and high cost of conventional lithium-ion batteries cannot fulfill the ever-increasing demands for portable electronic devices and electric vehicles.[1-5] Alternatively, owing to the high abundance and low cost of sulfur and particularly its ultrahigh theoretical capacity of 1675 mA h g^{-1}, lithium-sulfur (Li-S) batteries have been considered as one of the most promising candidates the next-generation electrical energy storage.[6-9] However, the rapid capacity degradation, low Coulombic efficiency, and short cycle life originating from polysulfide dissolution and migration remain challenging for the practical applications of Li-S batteries.[10-12] In recent years,

[a] *Materials Science and Engineering Program & Texas Materials Institute, The University of Texas at Austin, Austin, TX 78712, USA.*
E-mail: manth@austin.utexas.edu
[b] *State Key Laboratory of Electronic Thin Films and Integrated Devices, University of Electronic Science and Technology of China, Chengdu 610054, PR China*
E-mail: yfchen@uestc.edu.cn

Electronic Supplementary Information (ESI) available: [details of any supplementary information available should be included here]. See DOI: 10.1039/x0xx00000x

strenuous efforts have been pursued to mitigate those detrimental effects, including structural confinement design,[13-16] conductive composite material fabrication,[17-20] electrolyte modification,[21] multifunctional polar binder,[22] and interlayer configurations.[23-30]

Our previous reports have demonstrated that configuring interlayers between the separator and the sulfur cathode is an effective and convenient strategy to alleviate the shuttle effect.[23-30] Particularly, in order to avoid the weight and volume of free-standing interlayers, our group coated microporous carbon or carbon nanotubes on the separator itself.[26-30] Inspired by these work, some other carbonaceous materials (*e.g.*, graphene and carbon fiber) have been investigated as interlayer candidates as a barrier to suppress the shuttle effect of the lithium polysulfides (LiPSs).[31, 32] Recently, materials, such as polar metal oxides,[33] metal organic frameworks (MOF),[34] and metal nitrides,[35] have been proposed as functional interlayer barriers to chemically block the LiPSs shuttling. However, it is still a challenge to find an ideal interlayer for high-performance Li-S batteries. First, the carbonaceous materials can only physically block the LiPSs shuttling since their nonpolar surface possesses weak affinity for the polar LiPSs. Second, owing to the intrinsically low electrical conductivity of most of the polar materials, the immobilized LiPSs remain on the surface of the polar materials, which means the trapped active materials cannot be fully utilized and the rate capability will be compromised. Most importantly, to the best of our knowledge, most of those interlayers are fabricated by vacuum-filtration methods, which makes those polar materials easily stack together and thus form a very thick interlayer. Therefore, on the one hand, the transport of lithium ions will be limited by the thick polar interlayers, which is not desirable for fast insertion/de-insertion of Li ions and high rate capacity. On the other hand, the stacked thick interlayers, as an inactive material, will decrease the overall cell energy density. In this regard, it is crucial to design novel interlayers, which can not only be very thin for fast ion transport, but also provide sufficient surface to physically/chemically adsorb LiPSs for high electrochemical utilization.

Herein, we present, for the first time, well-aligned, hollow Co_9S_8 arrays *in-situ* grown on a Celgard (Co_9S_8-Celgard) separator as an efficient polysulfide barrier for high-performance Li-S cells, without any significant increase in the weight and volume. This novel concept/strategy of designing a multifunctional separator via *in-situ* grown polar and conductive materials (Co_9S_8 hollow arrays) on a commercial separator dramatically suppresses the shuttle effect of LiPSs and significantly improves the electrochemical performance of Li-S cells. Due to its well-designed structure, *in-situ* growth/transformation, and the polarity and high conductivity of Co_9S_8, the Li-S cell with the Co_9S_8-Celgard separator not only effectively blocks the LiPSs even with pure sulfur cathodes with a very high sulfur loading (5.6 mg cm^{-2}), but also delivers excellent specific capacity, outstanding rate capability, and remarkable cycling stability for an impressive number of 1,000 cycles. More importantly, the multifunctional Co_9S_8-Celgard separator also shows excellent electrochemical performance in a pouch cell, demonstrating that the Co_9S_8-Celgard separator is promising for practical applications. In essence, the novel design and *in-situ* growth of MOF-derived multifunctional Co_9S_8 layers are crucial to suppress the severe polysulfide diffusion and alleviate the shuttle effect of LiPSs. We believe that these contributions would promote greatly the development of modified separators, particularly the design and synthesis of multifunctional separators.

Experimental

Synthesis of MOF-Celgard

2.6 g of 2-methylimidazole and 1.17 g of $Co(NO_3)_2{\cdot}6H_2O$ were respectively dissolved in 80 mL of deionized water. Then, the above-mentioned solution was quickly mixed and a piece of Celgard was fixed on the beaker wall and immersed into the mixture for 5 h. The Celgard was then taken out, cleaned with deionized water, and vacuum dried overnight. The mass loading of the MOF interlayer was measured to be ~ 0.37 mg cm^{-2}. The mass loading level of MOF on the separator can be determined by comparing the weight of the separator before and after loading MOF.

Preparation of Co_9S_8-Celgard

A piece of MOF arrays on Celgard was immersed into an aqueous solution (60 mL) containing 0.6 g thioacetamide (TAA). After hydrothermal reaction at 100 °C for 6 h, the sample was taken out, washed with deionized water, and dried at 60 °C. The mass loading of Co_9S_8 interlayer was measured to be ~ 0.16 mg cm^{-2}. The mass loading level of Co_9S_8 on the separator can be determined by comparing the weight of the separator before and after loading Co_9S_8.

Preparation of Li_2S_6 and Co_9S_8-Celgard-Li_2S_6 for absorptivity measurements

A 0.05 M Li_2S_6 solution was prepared by dissolving elemental S and Li_2S in a molar ratio of 5 : 1 in 1,3-dioxolane and 1,2-dimethoxyethane (v/v = 1 : 1) at 65 °C with vigorous stirring for 24 h. Then, a piece of Co_9S_8-Celgard was added to 10 mL of Li_2S_6 solution to obtain the Co_9S_8-Celgard-Li_2S_6 solution. After 30 min, the precipitated product was dried. Finally, the Co_9S_8-Celgard-Li_2S_6 sample was obtained for XPS analysis. All the procedures were performed in an argon-filled glovebox.

Characterizations

The crystalline structure of the obtained samples was characterized by X-ray diffraction (XRD Rigaku D/MAX-rA diffractometer) with Cu Kα radiation. The morphology investigation was performed with a scanning electron microscope (FEI Quanta 650 SEM operated at 20 kV) and an energy dispersive X-ray (EDX) spectrometer to detect the elemental signals. Specific surface area measurements were obtained with an automated gas sorption analyzer (AutoSorb iQ2, Quantachrome Instruments). XPS analysis was performed with a Kratos Analytical spectrometer at room temperature with monochromatic Al Kα (1,486.6 eV) radiation. Fourier transform infrared (FT-IR) spectra were recorded on a Nicolet iS5 FT-IR spectrometer.

Electrochemical measurements

Each electrode contained 70 wt.% sulfur powder, 15 wt.% Super-P, and 15 wt.% polyvinylidene fluoride (PVDF). Coin-type (CR2032) cells were assembled in an Ar-filled glove box with lithium metal as the anode. Celgard 2500, MOF-Celgard, and Co_9S_8-Celgard were used as the separator. The electrolyte was composed of 1.85 M $LiCF_3SO_3$ in 1,3-dioxolane and 1,2-dimethoxyethane (v/v = 1:1) with 0.1 M $LiNO_3$ as additive. The pouch cell was sealed with an aluminum soft packaging film. The electrolyte-to-sulfur ratio for the coin cell and pouch cell was 10. An Arbin battery cycler was used to conduct the cycling performance between 1.8 and 2.8 V at room temperature.

Cyclic voltammetry (CV) measurements were evaluated with a VoltaLab PGZ 402 Potentiostat with a scan rate of 0.1 mV s^{-1} in the potential range of 1.8 and 2.8 V. Electrochemical impedance spectroscopy (EIS) data were collected with a CHI 660D electrochemical workstation in the frequency range of 100 kHz to 0.01 Hz. In this work, the specific capacity values were calculated on the basis of sulfur mass.

Results and discussion

The fabrication procedure is illustrated in **Fig. 1**a. First, the well-aligned cobalt-based 2D MOF nanowall arrays were *in-situ* grown on the Celgard (MOF-Celgard) through a facile solution method, which allows scalable production of the MOF-Celgard (**Fig. S1**). Then, the MOF-Celgard was chemically transformed to Co_9S_8-Celgard *via* a solvothermal sulfurization, which can be directly used as a multi-functional separator for Li-S batteries. It is noted that the color of the Co-MOF on Celgard (purple, Fig. S1) is completely changed to black after the solvothermal sulfurization (**Fig. S2**), confirming the full transformation of Co-MOF to Co_9S_8 form.

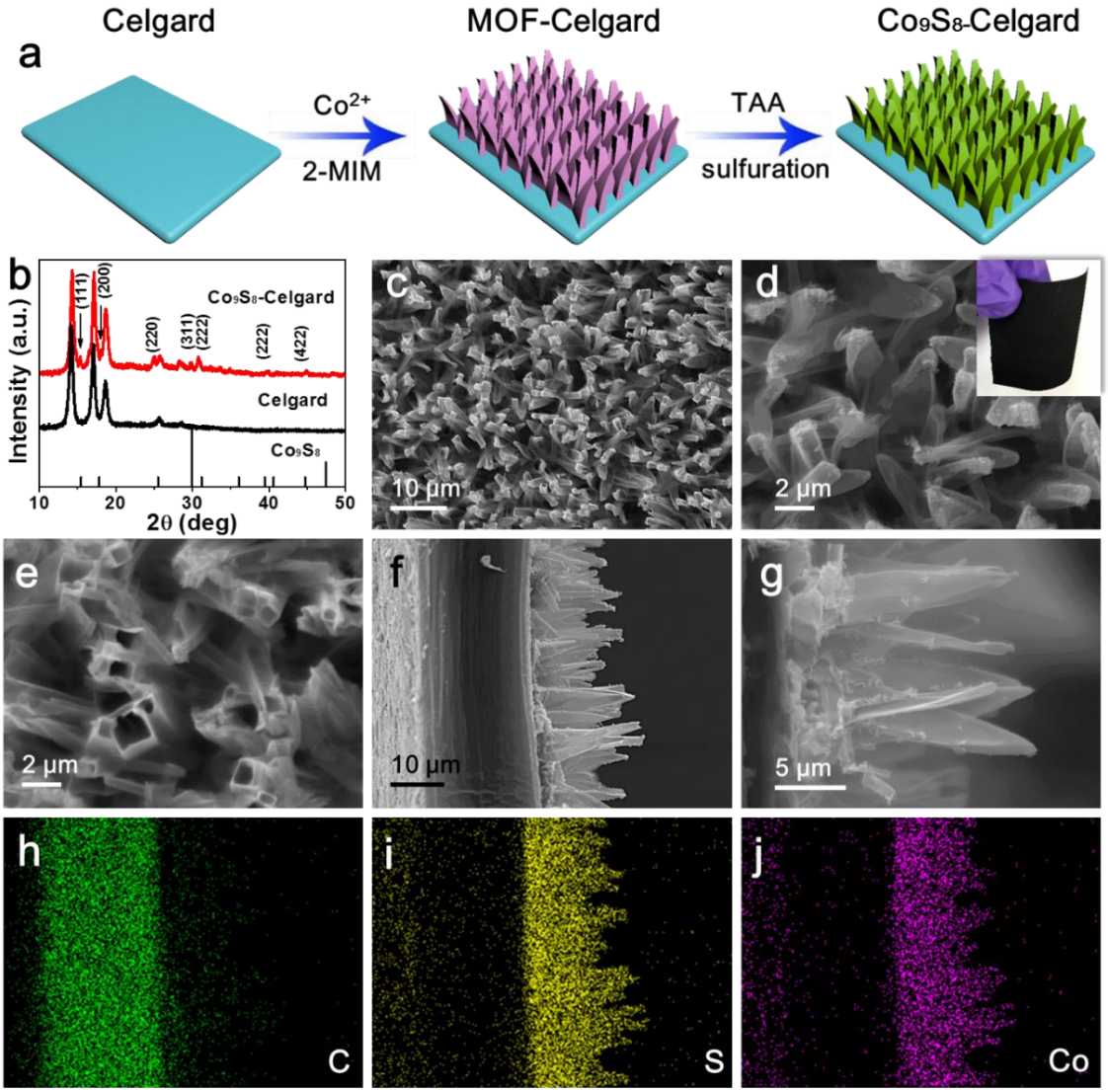

Fig. 1 (a) Schematic illustration of the synthesis process of Co_9S_8-Celgard. (b) XRD patterns of Co_9S_8, Celgard, and Co_9S_8-Celgard. (c and d) Top-surface morphology of Co_9S_8-Celgard at various magnifications. The inset shows a digital photo. (e) SEM image of Co_9S_8-Celgard after slight scratch. (f and g) Cross-sectional morphologies of Co_9S_8-Celgard, and the corresponding elemental mapping images of (h) carbon, (i) sulfur, and (j) cobalt.

The XRD pattern of MOF-Celgard (**Fig. S3**a) matches well with those of Celgard separator and MOF powder, which also agrees well with the previous reports.[36, 37] This evidently confirms the successful incorporation of MOF on the Celgard separator. The SEM images (Fig. S3b – 3d) show that the Co-MOF with a typical 2D morphology has been uniformly grown on the Celgard separator (**Fig. S4**). In addition, the corresponding elemental mapping images in Fig. S3h – 3i further illustrate the homogeneous elemental distribution of carbon and cobalt. As shown in Fig.1b, the characteristic peaks

of Co_9S_8 (JCPDS No. 19-0364) are clearly observed in Co_9S_8-Celgard, which indicates that MOF can be easily transformed into Co_9S_8 after a low-temperature (100 °C) solution-phase sulfurization treatment. From the top view SEM images of Co_9S_8-Celgard in Fig. 1c – 1d, the well-aligned Co_9S_8 nanowalls were vertically and uniformly grown on the Celgard after the sulfurization treatment. It should be noted that the Co_9S_8 arrays were grown on only one side of the separator, which faces the sulfur cathode. The other side of the separator is bare and same as the nomal separator. This means, similar to the cell with the normal separator, cell shorting will not occur with the Co_9S_8-modified separator. The photograph of a bent Co_9S_8-Celgard (inset of Fig. 1d) illustrates its good mechanical stability, and the corresponding SEM and elemental mapping images (**Fig. S5**) further demonstrate the uniform distribution of Co_9S_8 on the Celgard. The SEM (Fig. 1e) of Co_9S_8-Celgard after slight scratch indicates that the Co_9S_8 arrays have hollow nanoarchitecture. Since the LiPSs adsorption is proportional to the surface area of Co_9S_8,[38] such unique Co_9S_8 arrays with hollow nanoarchitecture ensure abundant adsorption interface for absorbing LiPSs. Specific surface area and pore size distribution results further confirm the high specific area and large pore volume (**Fig. S6**) of Co_9S_8. The formation of hollow Co_9S_8 arrays is mainly attributed to the Kirkendall effect resulting from the different diffusion rates of sulfur and cobalt species.[39] The cross-sectional morphologies of Co_9S_8-Celgard in Fig. 1f – 1g evidently show the robust physical connection between the Co_9S_8 arrays and the Celgard, indicating good mechanical stability. The photographs in **Fig. S7** and the **Media S1** evidence the robust connection between Celgard and Co_9S_8. The corresponding elemental mapping images in Fig. 1h – 1j further illustrate the homogeneous elemental distribution for carbon, sulfur, and cobalt. From the synthesis process and characterizations mentioned above, one can conclude that our method is facile, low cost, and scalable to *in-situ* grow well-aligned hollow Co_9S_8 arrays on Celgard as a multifunctional barrier.

In order to demonstrate the structural benefit of Co_9S_8-Celgard separator for blocking the LiPSs shuttling, a series of electrochemical characterizations were performed. The electrode, which contains 70 wt.% sulfur powder, 15 wt.% super-P, and 15 wt.% polyvinylidene fluoride (PVDF), was employed as a standard cathode (**Fig. S8**). As shown in **Fig. S9**, the cyclic voltammetry (CV) curves of the cells with the Co_9S_8-Celgard separator in the first three cycles were conducted at 0.1 mV s^{-1} in the potential range of 1.8 - 2.8 V. Two main reduction peaks are detected at 2.35 and 2.00 V in the first cathodic sweep, corresponding to the transformation of sulfur to long-chain LiPSs and ultimately to Li_2S.[40, 41] An oxidation peak is observed at 2.42 V during the successive anodic sweep, which is attributed to the reversible conversion of Li_2S to LiPSs and finally to sulfur.[42] During the repeated sweeps, the CV curves remain overlapping, indicating the prominent cyclic performance and reversible redox conversion. The plateaus in charge/discharge curves of the cells with the Co_9S_8-Celgard separator at C/10 rate match well with the peaks in the CVs as mentioned above and shown in **Fig. 2**a. More importantly, the well-overlapped voltage plateaus of the cells in 200 cycles verify the highly suppressed LiPSs shuttling. The charge/discharge curves of a cell with Co_9S_8 as the cathode is shown in **Fig. S10**, which reveals that Co_9S_8 has a very small capacity between 1.9 and 2.6 V. Its specific capacity (< 60 mA h g^{-1}) below 1.9 V is almost negligible compared to the large capacity of sulfur.

The long-term cyclability is a key factor to evaluate the cells with various separators. In this regard, the long-term cycling performances of the cells with the Celgard, MOF-Celgard, and Co_9S_8-Celgard separators were measured at a potential range of 1.8 - 2.8 V with the same sulfur loading of 2 mg cm^{-2} at C/10 rate (1C = 1,675 mA g^{-1}). As shown in Fig. 2b, the initial discharge capacity of the cell with Co_9S_8-Celgard separator approaches a high value of 1,385 mA h g^{-1}, and it retains a high discharge capacity of 1,190 mA h g^{-1} even after 200 cycles. It is noted that after 200 cycles, the capacity retention of the cell with the Co_9S_8-Celgard separator is as high as 85.9%, which is much higher than that of the control cell with the pristine Celgard separator (only ~ 10% capacity retention). It is noted that the difference between the performances of the cells with MOF-Celgard and Co_9S_8-Celgard seems only to be in early cycling. In order to further investigate such differences, we obtained the SEM image of the MOF-Celgard after 10 cycles, and the results are presented in **Fig. S14**. As shown in Fig. S14, the morphology of the MOF arrays changed a lot, converting to a smooth layer. Compared to MOF-Celgard, even after 200 cycles, the Co_9S_8 nanowalls still retained their original form (**Fig. S12** and **Fig. 13**). Thus, the difference in the early cycling might be attributed to the morphological changes of the MOF arrays. Importantly, the cells with the Co_9S_8-Celgard separator still retain 530 mA h g^{-1} after an impressive number of 1,000 cycles with an average capacity fading of only 0.039% per cycle. The pronounced cycling performance for an impressive number of 1,000 cycles with the Co_9S_8-Celgard separator further illustrates the advantage of the Co_9S_8-Celgard separator (Fig. 2e). The significant enhancement in electrochemical performance for the cell with the Co_9S_8-Celgard separator is mainly attributed to its remarkable suppression of the shuttling effect *via* the strong chemical and physical absorption for LiPSs to effectively block the active material within the cathode region. The morphologies of the lithium anodes in the cells with the bare Celgard separator, MOF-Celgard separator, and Co_9S_8-Celgard separators after 200 cycles (**Fig. S11**) evidently demonstrate that the Co_9S_8-Celgard separator is very effective to suppress the LiPSs shuttling.

Journal Name

ARTICLE

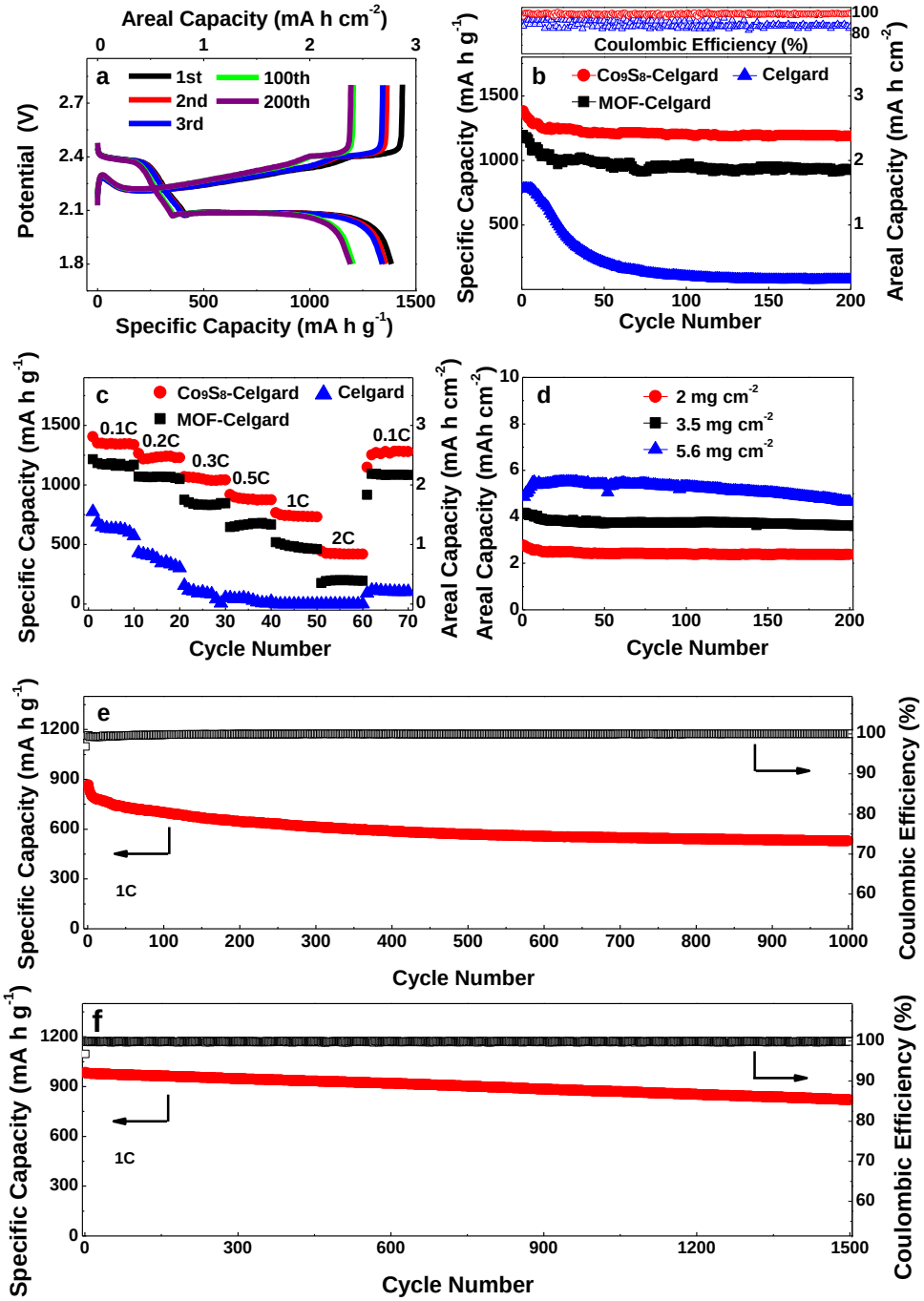

Fig. 2 (a) Charge/discharge profiles at C/10 rate. (b) Cyclic stability of the cells with the Celgard, MOF-Celgard, and Co_9S_8-Celgard separators at C/10 rate for 200 cycles. (c) Rate performances at various cycling rates with the Celgard, MOF-Celgard, and Co_9S_8-Celgard separators. (d) Cycling performances of Li-S cells with high sulfur-loading cathodes with Co_9S_8-Celgard separators. (e) Long term cycling performances of the Li-S cells with the Co_9S_8-Celgard separators at 1C rate for 1,000 cycles. (f) Long term cycling performances of the Li-S cells with the Co_9S_8-Celgard separators based on S/YSC@Fe_3O_4 cathode at 1C rate for 1,500 cycles.

Journal Name

ARTICLE

The cell employing Co_9S_8-Celgard separator also exhibits prominent rate capability under various cycling rates from C/10 to 2C rates, as shown in Fig. 2c. In comparison to the cell with the MOF-Celgard separator, the cell with the Co_9S_8-Celgard separator attains a high discharge capacity of 428 mA h g^{-1} at a high cycling rate of 2C. Such a result evidently indicates that the Co_9S_8-Celgard separator can not only significantly mitigate the shuttle effect through the strong chemical and physical adsorption to LiPSs, but also accelerate the redox kinetics of polysulfides in liquid phase.[38, 43, 44] In particular, when the cycling rate switches back to C/10 rate, the capacity of the cells with the Co_9S_8-Celgard separator can be recovered to 1,270 mA h g^{-1}, indicating its good mechanical stability and the excellent LiPSs restriction by the Co_9S_8-Celgard separator. The post-mortem SEM analysis (Fig. S12 - Fig. S14) further demonstrates that the stable structural integrity of the Co_9S_8-Celgard separator.

As shown in Fig. 2d and **Fig. S15**, the feasibility of the Co_9S_8-Celgard separator is extended by augmenting the sulfur loading to 5.6 mg cm^{-2}. Impressively, the cells employing the Co_9S_8-Celgard separators with a sulfur loading of up to 5.6 mg cm^{-2} can still deliver a high discharge capacity of 985 mA h g^{-1}, which corresponds to a high areal capacity of 5.5 mA h cm^{-2}. Even after 200 cycles, the cells employing the Co_9S_8-Celgard separator exhibits pronounced cyclic performance with a capacity retention of up to 84.3%.

In order to fully demonstrate the advantage of the Co_9S_8-Celgard, a cathode consisting of well-designed yolk-shelled carbon@Fe_3O_4 (YSC@Fe_3O_4) nanoboxes loaded with sulfur (S/YSC@Fe_3O_4) was employed, which was an optimized cathode in our previous report.[17] As shown in Fig.2f, the cell with Co_9S_8-Celgard and YSC@Fe_3O_4 cathode delivers a high initial capacity of 986 mA h g^{-1} at 1C rate with a capacity retention of as as high as 83.2 % even after 1,500 cycles. Such a pronounced cycling performance clearly illustrates the outstanding confinement capability of the Co_9S_8-Celgard towards LiPSs.

To further demonstrate the potential of the Co_9S_8-Celgard separator for practical applications, pouch cells were assembled (**Fig. 3**a – 3d). Here, the areal loading of sulfur with the pure sulfur electrode was 2 mg cm^{-2}, and the area was 12.0 cm^{-2}. As shown in Fig. 3d, the pouch cell with the Co_9S_8-Celgard separator delivers 1,185 mA h g^{-1} and remains stable after 30 cycles, which is the best performance reported for pouch Li-S cells in the literature. Such an excellent electrochemical performance of the pouch cells further illustrates that the Co_9S_8-Celgard separator can act as a multifunctional barrier in practical Li-S cells.

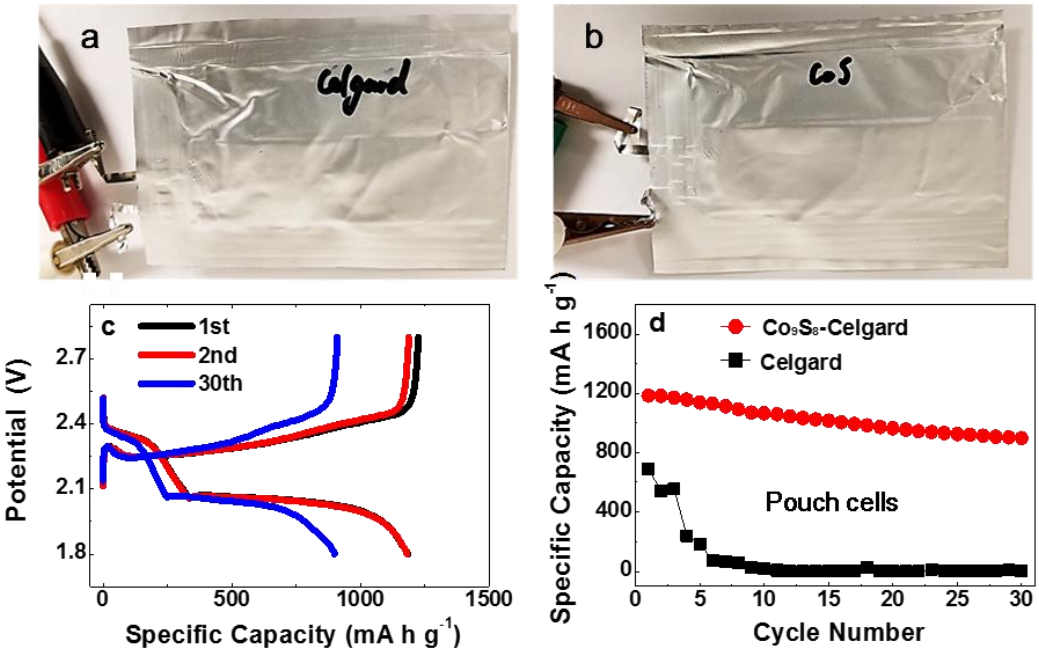

Fig. 3 Photos of pouch cells with (a) Celgard and (b) Co_9S_8-Celgard separators. (c) Charge/discharge profiles of pouch Li-S cells with Co_9S_8-Celgard separator at C/10 rate. (d) Cycling performances of pouch Li-S cells with Celgard and Co_9S_8-Celgard separators.

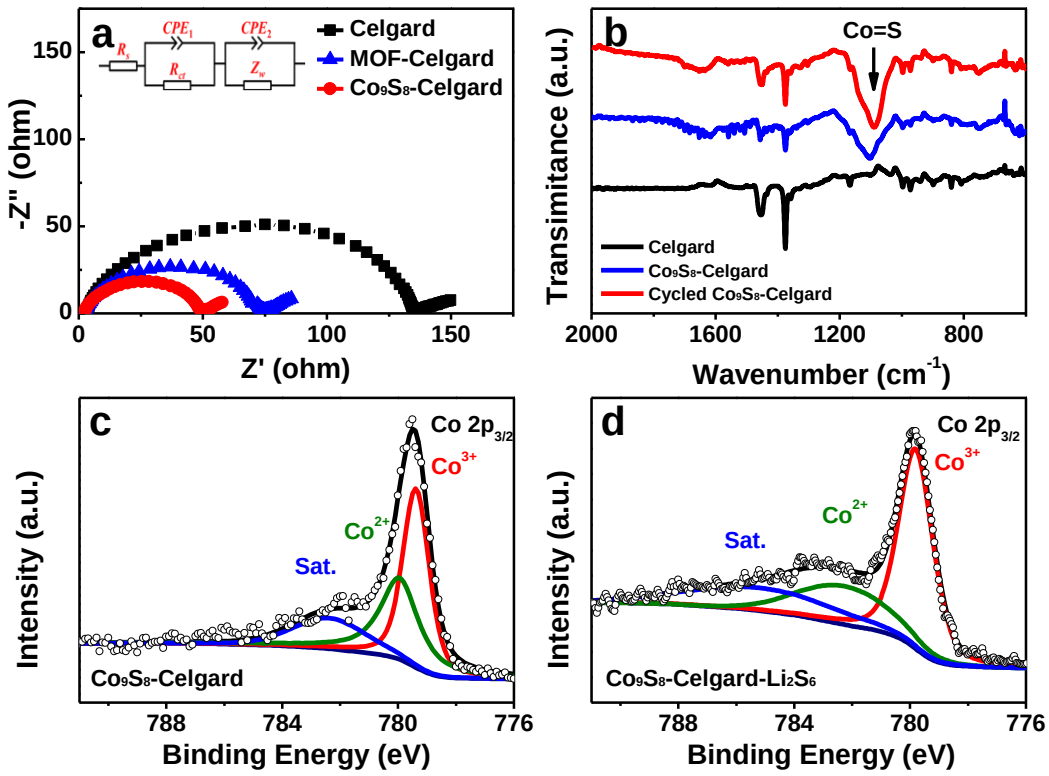

Fig. 4 (a) EIS plots of the cycled cells with Celgard, MOF-Celgard, and Co_9S_8-Celgard separators. (b) IR spectra of the Co_9S_8-Celgard separators before and after the electrochemical process. High-resolution XPS Co $2p_{3/2}$ spectra of (c) Co_9S_8-Celgard and (d) Co_9S_8-Celgard-Li_2S_6.

The electrochemical impedance spectroscopy (EIS) spectra of the cells with the Co_9S_8-Celgard, MOF-Celgard, and pristine Celgard separators are shown in **Fig. 4**a. The high-frequency semicircles and low-frequency sloping lines in the Nyquist curves correspond to the charge-transfer resistance (R_{ct}) and the lithium ion diffusion resistance within the electrodes, respectively. It is easily observed that the cells with Co_9S_8-Celgard after the cycling tests shows the lowest R_{ct} compared to those with MOF-Celgard and pristine Celgard separators, suggesting that the lithium metal paired with Co_9S_8-Celgard is coated less by LiPSs and potentially has less dendrites, as indicated by the morphology of lithium metal after 200 cycles in Fig. S11. Notably, the charge-transfer resistance of the fresh cells with the Co_9S_8-Celgard separator is lower than that of the cells with the bare Celgard separator (**Fig. S16**), indicating that the localized charge transfer of sulfur species in the cells with the Co_9S_8-Celgard separator is better than that of the cells with the Celgard separator. The results indicate that the Co_9S_8-Celgard separator can effectively confine polysulfides, thus improving the utilization of active material sulfur. Therefore, the cells with the Co_9S_8-Celgard separator exhibit better rate performance than the cells with the Celgard separator.

To further reveal the mechanism of Co_9S_8-Celgard separator for blocking LiPSs shuttling, the Co_9S_8-Celgard separators before and after cycling were examined by FT-IR (Fig. 4b). The strong peak at 1,101 cm^{-1} in the fresh Co_9S_8-Celgard separator is ascribed to the Co = S stretching,[45] indicating the existence of cobalt sulfide in the modified separator, which matches well with the XRD analysis (Fig. 2a). Apparently, the Co = S peak in the cycled Co_9S_8-Celgard separator slightly shifts and becomes broaden as compared to the fresh one, indicating the possible formation of a chemical interaction between Co_9S_8 and LiPSs.[46] The slight changes in the IR spectra of the MOF-Celgard separators before and after cycling also illustrate that the MOF can provide chemical interaction with LiPSs (**Fig. S17**).

The chemical interaction between Co_9S_8 and LiPSs was quantitatively evaluated by the X-ray photoelectron spectroscopy (XPS) analysis, which can easily identify the state of cobalt in Co_9S_8 after contacting with LiPSs. The Li_2S_6 was chosen to represent the LiPSs. Fig. 4c - 4d show the XPS spectra at the Co $2p_{3/2}$ region of Co_9S_8-Celgard and Co_9S_8-Celgard-Li_2S_6, respectively. The Co $2p_{3/2}$ spectrum of Co_9S_8-Celgard shows two components at 779.4 and 780 eV, ascribed, respectively, to Co^{3+} and Co^{2+}, which correspond to two types of cobalt that occupy distinct lattice sites (octahedral and tetrahedral, respectively). After contacting with Li_2S_6, the Co $2p_{3/2}$ peaks of Co_9S_8-Celgard-Li_2S_6 shift towards higher binding energy, which indicate the strong chemical interaction between Li_2S_6 and Co atoms.[38, 47] It evidently indicates that the Co_9S_8-Celgard has stronger affinity to LiPSs through the chemical adsorption by Co_9S_8, which is also in good agreement with the computational results of the interaction between Co_9S_8 and lithium polysulfide in the literature.[48]

In order to visually demonstrate the LiPSs blocking ability of the Co_9S_8 interlayer in Li-S cell, glass cells were set up (**Fig. 5**). The left chamber was filled with LiPSs (Li_2S_6) solution in

DOL/DME solvent, and the right chamber was filled with DOL/DME solvent without Li_2S_6. These two chambers were separated by the pristine Celgard separator (top pannel), and the Co_9S_8 modified Celgard separator (bottom pannel), respectively. From the top panel of the Fig. 5, for the cell with pristine Celgard separator, one can observe that the right chamber changed to yellow-brown after 48 h, which shows the LiPSs can easily diffuse across the pristine separator. In sharp contrast, the glass cell with the Co_9S_8-Celgard separator shows no obvious color change in the right chamber (see the bottom panel of Fig. 5), which suggests that the shuttle of LiPSs is significantly mitigated by the Co_9S_8 modified separator.

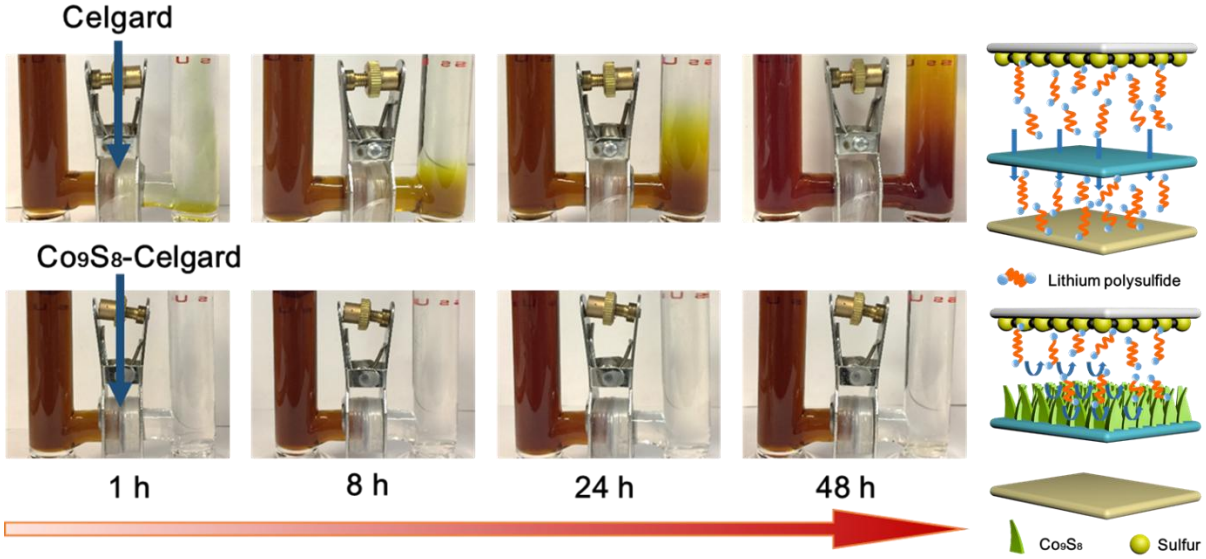

Fig. 5. Photographs of glass cells with LiPSs (Li_2S_6) in DOL/DME solution and pure DOL/DME solvent in left and right chambers, respectively, separated by Celgard (top panel) and the Co_9S_8-Celgard separators (bottom panel) and the improvement mechanism of the Co_9S_8-Celgard separator during the charge/discharge processes.

Conclusions

In summary, we have designed and prepared a novel interlayer with well-aligned hollow Co_9S_8 arrays *in-situ* grown on Celgard separator as an efficient polysulfide barrier for high-performance Li-S cells. During the electrochemical process, the well-aligned multifunctional Co_9S_8 interlayer plays an important role to effectively block the LiPSs shuttling and fully utilize the sulfur cathode. The Co_9S_8 modified separator allows the Li-S cells employing pure sulfur cathodes to attain enhanced cycling stability and a lower capacity-fade rate with high sulfur loading (up to 5.6 mg cm^{-2}). In addition, the excellent electrochemical performance of the pouch cells further illustrates that the Co_9S_8-Celgard separator can act as a multifunctional barrier in practical Li-S cells. This work provides a new perspective to design high-performance Li-S batteries by constructing polar interlayers as a multifunctional barrier with high conductivity and large surface area.

Conflicts of interest

There are no conflicts to declare.

Acknowledgements

This work was supported by the U.S. Department of Energy, Office of Basic Energy Sciences, Division of Materials Science and Engineering under award number DE-SC000597. One of the authors (J. H) thanks the China Scholarship Council (Grant No. 201606070032) for the award of a fellowship.

Notes and references

1 M. Yu, J. Ma, H. Song, A. Wang, F. Tian, Y. Wang, H. Qiu, R. Wang, *Energy Environ. Sci.* 2016, **9**, 1495.

2 M. Barghamadi, A. S. Best, A. I. Bhatt, A. F. Hollenkamp, M. Musameh, R. J. Rees, T. Rüther, *Energy Environ. Sci.* 2014, **7**, 3902.

3 J. Zhou, R. Li, X. Fan, Y. Chen, R. Han, W. Li, J. Zheng, B. Wang, X. Li, *Energ. Environ. Sci.* 2014, **7**, 2715.

4 G. Zhou, D. Wang, F. Li, P. Hou, L. Yin, C. ô. L. G. Liu, I. R. Gentle, H. Cheng, *Energ. Environ. Sci.* 2012, **5**, 8901.

5 J. He, Y. Chen, W. Lv, K. Wen, Z. Wang, W. Zhang, Y. Li, W. Qin, W. He, *ACS Nano* 2016, **10**, 8837.

6 G. Zhou, F. Li, H. Cheng, *Energ. Environ. Sci.* 2014, **7**, 1307.

7 J. He, W. Lv, Y. Chen, K. Wen, C. Xu, W. Zhang, Y. Li, W. Qin, W. He, *ACS Nano* 2017, **11**, 8144.

8 F. Wu, J. T. Lee, N. Nitta, H. Kim, O. Borodin, G. Yushin, *Adv. Mater.* 2015, **27**, 101.

9 Q. Pang, L. F. Nazar, *ACS Nano* 2016, **10**, 4111.

10 Y. Li, J. Fan, M. Zheng, Q. Dong, *Energy Environ. Sci.* 2016, **9**, 1998.

11 Y. You, W. Zeng, Y. Yin, J. Zhang, C. Yang, Y. Zhu, Y. Guo, *J. Mater. Chem. A* 2015.

12 X. Ye, J. Ma, Y. Hu, H. Wei, F. Ye, *J. Mater. Chem. A* 2016, **4**, 775.

13 S. Xin, L. Gu, N. Zhao, Y. Yin, L. Zhou, Y. Guo, L. Wan, *J. Am. Chem.*

Soc. 2012, **134**, 18510.
14 G. Zhou, Y. Zhao, C. Zu, A. Manthiram, *Nano Energy* 2015, **12**, 240.
15 J. He, Y. Chen, A. Manthiram, *iScience* 2018, 36.
16 C. Chang, S. Chung, A. Manthiram, *Mater. Horiz.* 2017, **4**, 249.
17 J. He, L. Luo, Y. Chen, A. Manthiram, *Adv. Mater.* 2017, **29**, 1702707.
18 J. He, Y. Chen, W. Lv, K. Wen, C. Xu, W. Zhang, Y. Li, W. Qin, W. He, *ACS Nano* 2016, **10**, 10981.
19 L. Ji, M. Rao, H. Zheng, L. Zhang, Y. Li, W. Duan, J. Guo, E. J. Cairns, Y. Zhang, *J. Am. Chem. Soc.* 2011, **133**, 18522.
20 J. He, Y. Chen, W. Lv, K. Wen, C. Xu, W. Zhang, W. Qin, W. He, *ACS Energy Letters* 2016, **1**, 820.
21 Y. Su, Y. Fu, T. Cochell, A. Manthiram, *Nat. Commun.* 2013, **4**, 2985.
22 W. Chen, T. Qian, J. Xiong, N. Xu, X. Liu, J. Liu, J. Zhou, X. Shen, T. Yang, Y. Chen, C. Yan, *Adv. Mater.* 2017, **29**, 1605160.
23 M. Liu, Q. Li, X. Qin, G. Liang, W. Han, D. Zhou, Y. He, B. Li, F. Kang, *Small* 2017, **13**, 1602539.
24 Z. Xiao, Z. Yang, L. Wang, H. Nie, M. Zhong, Q. Lai, X. Xu, L. Zhang, S. Huang, *Adv. Mater.* 2015, **27**, 2891.
25 Y. Su, A. Manthiram, *Nat. Commun.* 2012, **3**, 1166.
26 Y. Su, A. Manthiram, *Chem. Commun.* 2012, **48**, 8817.
27 A. Manthiram, Y. Fu, S. Chung, C. Zu, Y. Su, *Chem. Rev.* 2014, **114**, 11751.
28 S. Chung, A. Manthiram, *Adv. Mater.* 2014, **26**, 7352.
29 S. Chung, A. Manthiram, *Adv. Mater.* 2014, **26**, 1360.
30 C. Chang, S. Chung, A. Manthiram, *Small* 2016, **12**, 174.
31 W. Lin, Y. Chen, P. Li, J. He, Y. Zhao, Z. Wang, J. Liu, F. Qi, B. Zheng, J. Zhou, *J. Electrochem. Soc.* 2015, **162**, A1624.
32 J. Wang, Y. Yang, F. Kang, *Electrochim. Acta* 2015, **168**, 271.
33 W. Li, J. Hicks-Garner, J. Wang, J. Liu, A. F. Gross, E. Sherman, J. Graetz, J. J. Vajo, P. Liu, *Chem. Mater.* 2014, **26**, 3403.
34 S. Bai, X. Liu, K. Zhu, S. Wu, H. Zhou, *Nature Energy* 2016, **1**, 16094.
35 T. Zhou, W. Lv, J. Li, G. Zhou, Y. Zhao, S. Fan, B. Liu, B. Li, F. Kang, Q. Yang, *Energy Environ. Sci.* 2017, **10**, 1694.
36 G. Fang, J. Zhou, C. Liang, A. Pan, C. Zhang, Y. Tang, X. Tan, J. Liu, S. Liang, *Nano Energy* 2016, **26**, 57.
37 C. Guan, W. Zhao, Y. Hu, Z. Lai, X. Li, S. Sun, H. Zhang, A. K. Cheetham, J. Wang, *Nanoscale Horiz* 2017, **2**, 99.
38 J. Pu, Z. Shen, J. Zheng, W. Wu, C. Zhu, Q. Zhou, H. Zhang, F. Pan, *Nano Energy* 2017, **37**, 7.
39 J. Liu, C. Wu, D. Xiao, P. Kopold, L. Gu, P. A. van Aken, J. Maier, Y. Yu, *Small* 2016, **17**, 201503821.
40 J. He, Y. Chen, P. Li, F. Fu, Z. Wang, W. Zhang, *J. Mater. Chem. A* 2015, **3**, 18605.
41 J. He, K. Zhou, Y. Chen, C. Xu, J. Lin, W. Zhang, *Mater. Today Energy* 2016, **1-2**, 11.
42 W. Zhou, Y. Yu, H. Chen, F. J. DiSalvo, H. D. Abruña, *J. Am. Chem. Soc.* 2013, **135**, 16736.
43 Q. Pang, D. Kundu, L. F. Nazar, *Materials Horizons* 2016, **3**, 130.
44 Z. Yuan, H. Peng, T. Hou, J. Huang, C. Chen, D. Wang, X. Cheng, F. Wei, Q. Zhang, *Nano Lett.* 2016, **16**, 519.
45 M. Jin, S. Lu, L. Ma, M. Gan, Y. Lei, X. Zhang, G. Fu, P. Yang, M. Yan, *J. Power Sources* 2017, **341**, 294.
46 X. Meng, J. Deng, J. Zhu, H. Bi, E. Kan, X. Wang, *Sci. Rep.-UK* 2016, **6**, 21717.
47 T. Chen, Z. Zhang, B. Cheng, R. Chen, Y. Hu, L. Ma, G. Zhu, J. Liu, Z. Jin, *J. Am. Chem. Soc.* 2017, **139**, 12710.
48 T. Chen, R. Chen, L. Ma, B. Cheng, Y. Hu, G. Zhu, Y. Wang, J. Liang, Z. Tie, J. Liu, Z. Jin, *Nano Energy* 2017, **38**, 239.

Table of Content Entry